

Evaluation of the Impact of View Differentiation and Backprojection Weight in Circle-plus-Line Cone-Beam Tomography

Stefan Hoppe, *Student Member, IEEE*, Frank Dennerlein, *Student Member, IEEE*, Günter Lauritsch, Joachim Hornegger, and Frédéric Noo, *Member, IEEE*,

Abstract—Recently, we proposed a new view differentiation scheme for analytical cone-beam reconstruction formulae that demonstrated a strong robustness to changes in the data acquisition geometry and to coarse view sampling, unlike former differentiation schemes. We incorporated this new scheme into the Katsevich reconstruction formula for the circle-plus-line trajectory. We also implemented an alternative Katsevich formula for the same trajectory, where the view differentiation step was eliminated by using integration by parts. This work evaluates both formulae in terms of resolution performance, noise performance, visual image quality and computational effort. We also evaluate the impact of the z-sampling on the line segment. Experiments are presented from simulated cone-beam data. The experiments show that the view differentiation approach with the new view differentiation scheme achieves similar image quality as the integration-by-part approach while being at the same time much more efficient.

Index Terms—Cone-Beam Reconstruction, View Differentiation, Integration by Parts.

I. INTRODUCTION

In computed tomography (CT), accurate cone-beam (CB) reconstruction formulae often involve the computation of a view-dependent data differentiation step, called view differentiation (VD) here, which may be suboptimal in terms of both spatial resolution as well as image quality. A common way therefore was to eliminate the differentiation step in the reconstruction formula by using integration by parts (IBP) [1],[2],[3],[4]. However, although IBP seems to be attractive in terms of resolution and image quality [2],[5], the resulting reconstruction formulae often involve several different filter terms which have to be backprojected separately with different backprojection weights, making such formulae less efficient than conventional one-term filtered backprojection (FBP) approaches. Moreover, in contrast to VD, some of those terms assign second order backprojection weights to a given voxel.

Recently, we proposed a new VD scheme that demonstrated a strong robustness to changes in the data acquisition geometry and to coarse view sampling, unlike former differentiation schemes; see [6] for details.

In this work, we focus on the circle-plus-line trajectory. We evaluate both the new VD scheme and the IBP approach with

S. Hoppe and J. Hornegger are with the Institute of Pattern Recognition (LME), University of Erlangen-Nuremberg, Erlangen, Germany.

F. Noo and F. Dennerlein are with the Department of Radiology (UCAIR), University of Utah, Salt Lake City, UT, USA.

G. Lauritsch is with the Siemens AG, Medical Solutions, Forchheim, Germany.

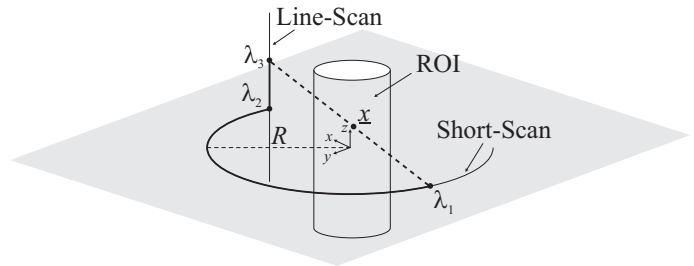


Fig. 1. The circle-plus-line trajectory is shown. To reconstruct a point \underline{x} inside the region of interest (ROI), backprojection is performed from λ_1 to λ_3 .

respect to resolution performance, noise performance, visual image quality, computational effort and the impact of the z-sampling on the line segment, using Katsevich's reconstruction formula [7] as a starting point. Experiments are presented from simulated CB data.

The paper is organized as follows. In Section II, we review the reconstruction formula for the circle-plus-line trajectory and show how that formula has to be modified to eliminate the view differentiation step by using integration by parts. Experiments are presented in Section III. Section IV summarizes our results.

II. RECONSTRUCTION FORMULAE

The task in image reconstruction is to recover the density of an object $f(\underline{x})$ given a set of line integrals through this object:

$$g(\lambda, \underline{\alpha}) = \int_0^\infty f(\underline{a}(\lambda) + t\underline{\alpha}) dt, \quad (1)$$

where λ denotes the source trajectory parameter, $\underline{a}(\lambda)$ describes the corresponding source position, and where $\underline{\alpha}$ denotes the direction of the line integral.

A. VD Katsevich Circle-plus-Line

With the geometry as in Figure 1, the VD reconstruction formula for the circle-plus-line trajectory can be compactly written as follows

$$f(\underline{x}) = \frac{1}{2\pi^2} \int_{\lambda_1}^{\lambda_3} \frac{1}{R - \underline{x} \cdot \underline{e}(\lambda)} g_1(\lambda, \underline{\alpha}) \Big|_{\underline{\alpha} = \frac{\underline{x} - \underline{a}(\lambda)}{\|\underline{x} - \underline{a}(\lambda)\|}} d\lambda, \quad (2)$$

where R is the radius of the circle scan, $\underline{e}(\lambda)$ is a unit vector which is orthogonal to the detector plane, pointing from the

detector towards the object. The term $g_1(\lambda, \underline{\alpha})$ was obtained by first computing $\frac{\partial}{\partial \lambda} g(\lambda, \underline{\alpha})$ using the new view differentiation scheme of [6], followed by a cosine weighting, performing then Hilbert filtering along predefined filter lines, followed by cosine post weighting; see [7].

B. IBP Katsevich Circle-plus-Line

Using IBP, equation (2) becomes

$$\begin{aligned}
 f(\underline{x}) = & \frac{1}{2\pi^2} \left[\frac{g_2(\lambda_1, \underline{\alpha})}{R - \underline{x} \cdot \underline{e}(\lambda_1)} + \frac{g_2(\lambda_3, \underline{\alpha})}{R - \underline{x} \cdot \underline{e}(\lambda_3)} \right. \\
 & - DR \int_{\lambda_1}^{\lambda_2} \frac{g_3(\lambda, \underline{\alpha})}{(R - \underline{x} \cdot \underline{e}(\lambda))^2} d\lambda \\
 & - \frac{1}{D} \int_{\lambda_1}^{\lambda_2} \frac{g_4(\lambda, \underline{\alpha})}{R - \underline{x} \cdot \underline{e}(\lambda)} d\lambda \\
 & + D \int_{\lambda_2}^{\lambda_3} \frac{g_5(\lambda, \underline{\alpha})}{(R - \underline{x} \cdot \underline{e}(\lambda))^2} d\lambda \\
 & \left. + \int_{\lambda_2}^{\lambda_3} \frac{g_6(\lambda, \underline{\alpha})}{R - \underline{x} \cdot \underline{e}(\lambda)} d\lambda \right]_{\underline{\alpha} = \frac{\underline{x} - \underline{a}(\lambda)}{\|\underline{x} - \underline{a}(\lambda)\|}}, \quad (3)
 \end{aligned}$$

where D denotes the source-to-detector distance. The terms $g_i(\lambda, \underline{\alpha})$ were computed from $g(\lambda, \underline{\alpha})$ by performing first cosine weighting and then basically applying the following steps in the given order: Hilbert filtering for $g_2(\lambda, \underline{\alpha})$; ramp filtering for $g_3(\lambda, \underline{\alpha})$; vertical gradient computation for $g_4(\lambda, \underline{\alpha})$; Hilbert filtering for $g_5(\lambda, \underline{\alpha})$; vertical gradient computation and integration along the filter lines for $g_6(\lambda, \underline{\alpha})$. Additionally, for all $g_i(\lambda, \underline{\alpha})$, cosine post weighting was applied. Note that the terms including $g_3(\lambda, \underline{\alpha})$ and $g_5(\lambda, \underline{\alpha})$ assign to each voxel second order backprojection weights.

III. EXPERIMENTS AND RESULTS

For the following experiments, we used a classical CT scanner geometry with $R = 570$ mm, $D = 1040$ mm and an isotropic detector pixel size of 1.4083 mm. If not specified otherwise in the text, we used a detector of size 1200×800 pixels (rows \times columns); we used an angular range of 236° (760 projections) for the circle scan and a length of 160 mm (200 projections) for the line scan.

A. Resolution Performance

To measure the achievable resolution of VD and IBP, we simulated various spheres with radius 0.15 mm (using 14×14 subsamples for each detector value) along four distinct curves through the ROI, see Figure 2. For the curves 1 to 3, the detector size was 51×761 pixels and for curve 4, the detector size was 801×401 pixels such that all spheres corresponding to the same curve were covered by the field of view. Each sphere was reconstructed within a cube of 64^3 voxels with a side length of 0.04 mm. Figure 3 shows the resulting full width half maximum (FWHM) values together with the standard deviation. For each sphere, the FWHM value was computed by evaluating the average intensity profile for 2592 half-lines which radiated from the center of the sphere with angle increments of 5° in every direction.

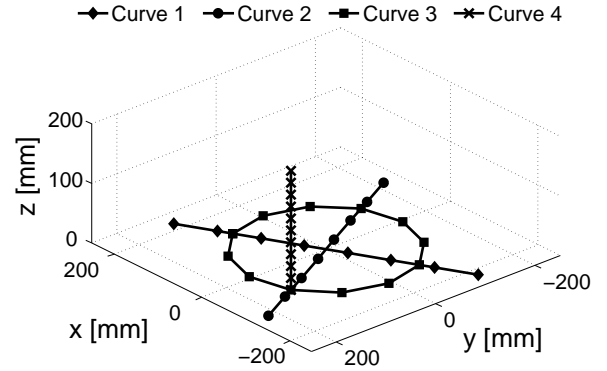


Fig. 2. The FWHM values were computed for the depicted spheres along curve 1 to 4. Curve 1 is parallel to a line connecting the end points of the short-scan, see trajectory in Figure 1.

From Figure 3 we observe that the IBP approach offers a slightly higher resolution than the VD approach, at least in remote off-center regions. The most significant difference in resolution is of 3.9%, corresponding to a difference of 0.032 mm over an overall mean FWHM value of 0.828 mm.

B. Noise Performance

To evaluate the noise performance, we simulated a modified FORBILD thorax phantom with an enlarged body contour (490 mm by 280 mm, shifted by 20 mm along y) using 3×3 subsamples for each detector value. We considered 1000 different Poisson noise realizations. Figure 4 shows the voxel-wise ratio of the standard deviation of IBP over VD for the slice $z = 0$. The slice consists of 512^2 voxels of side length 1.0 mm.

The results show that with the VD formula using the new view differentiation scheme, we obtain a significantly lower standard deviation at the borders of the object. The highest difference is 33.83% for a voxel at $d = 223.84$ mm away from the origin.

C. Visual Image Quality

Comparison between both VD and IBP reconstructions are shown in Figure 5 for the modified FORBILD thorax phantom (see Section III-B) and in Figure 6 for a single noisy data set of the same phantom.

The visual inspection of the obtained reconstruction results without noise shows that both formulae achieve overall the same visual image quality. In the presence of noise however, we see that the images obtained from the VD formula appear far more homogeneous than those obtained with the IBP formula.

D. Computational Effort

Table I shows the computing times obtained by running C implementations of both reconstruction formulae on a 64-bit AMD Opteron CPU with 2.0 GHz, 1 MB cache and 7 GB RAM, by reconstructing a volume consisting of 512^3 voxels of side length 1.0 mm.

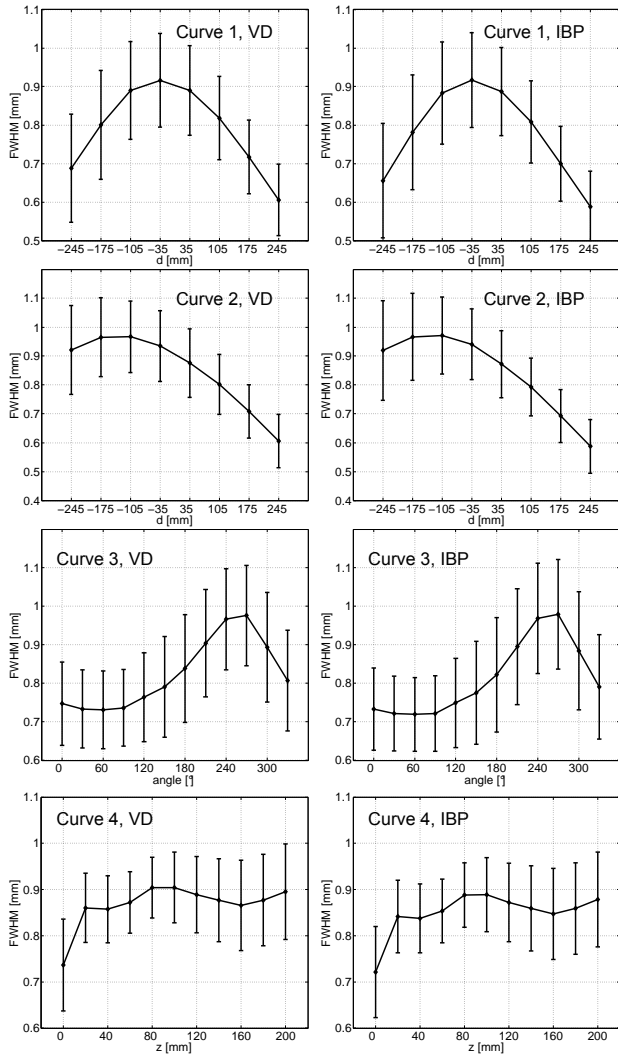


Fig. 3. FWHM values along curve 1 (top) to 4 (bottom) for VD (left) and IBP (right), see setup in Figure 2.

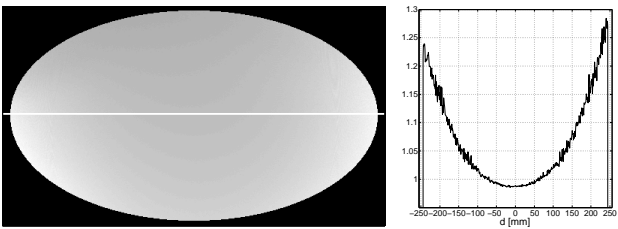


Fig. 4. (Left) Voxel-wise standard deviation ratio (IBP over VD). (Right) Plot along the depicted line.

From the the difference in computing time between the two methods, we see that the VD formula can be implemented almost twice as fast as the IBP approach. This difference is dominated by the circle part of the trajectory, where the computing time ratio of VD over IBP is less than 60%.

E. Impact of z -Sampling on the Line

To evaluate the robustness and stability of the two reconstruction formulae for a varying number of sampling points on the line segment, we simulated three different data sets of

	Circle	Line	Circle-plus-Line
VD	7239.04 [sec]	3988.57 [sec]	11227.61 [sec]
IBP	12337.38 [sec]	4442.17 [sec]	16779.55 [sec]
VD/IBP	58.68 %	89.79 %	66.91 %

TABLE I
COMPUTING TIMES FOR THE RECONSTRUCTION OF A 512^3 Voxel VOLUME.

	200 proj.	100 proj.	50 proj.
$x = 0$ mm	1.84	1.81	1.79
$y = -80$ mm	2.00	1.99	1.96

TABLE II
AVERAGE STANDARD DEVIATION RATIOS OF IBP OVER VD.

the modified FORBILD thorax phantom (see Section III-B) for the line segment. These data sets consist of 200, 100, and 50 projections, respectively. In each case, the line length is 160 mm, reaching 80 mm above and 80 mm below the plane of the circle scan. We simulated only one data set for the circle segment with 760 projections, corresponding to a short-scan of 236° , the same range we used for all the other experiments.

Figure 7 shows two reconstructed orthogonal slices for each case, without noise. Each slice consists of 256^2 voxels of side length 2.0 mm. The slices have been chosen to include high frequencies, especially in the z -direction, the direction where the sampling on the line varies.

Figure 8 shows the standard deviation images for the same slices for all three sampling rates. Those images were obtained from 20 different Poisson noise realizations. However, since this study is about the influence of the sampling on the line, only the line contribution was disturbed by noise while the circle contribution was noise-free.

From the noiseless experiment we observe that there is almost no difference in visual image quality between the VD and the IBP approach. The computed standard deviation images show that (i) for each sampling rate, the VD formula offers a significantly lower standard deviation in both orthogonal slices and (ii) that the standard deviation increases with decreasing sampling on the line. Observation (i) highlights, as Figure 4 did, that VD and IBP propagate noise in a significantly different way. Observation (ii) is expected since we apply only 25% of the dose when using a sampling of 50 projections compared to the case where we have 200 projections on the line.

Table II shows that the ratio of the mean standard deviations of IBP over VD is for all three sampling rates close to 180% for the slice $z = 0$ mm and close to 200% for the slice $y = -80$ mm, which means that for an average reconstructed pixel of the regarded slices, the standard deviation offered by the IBP approach is almost twice as high as for the VD approach. On the other hand we observe that IBP offers a maximal improvement in resolution of only 3.9%, c.f. Section III-A.

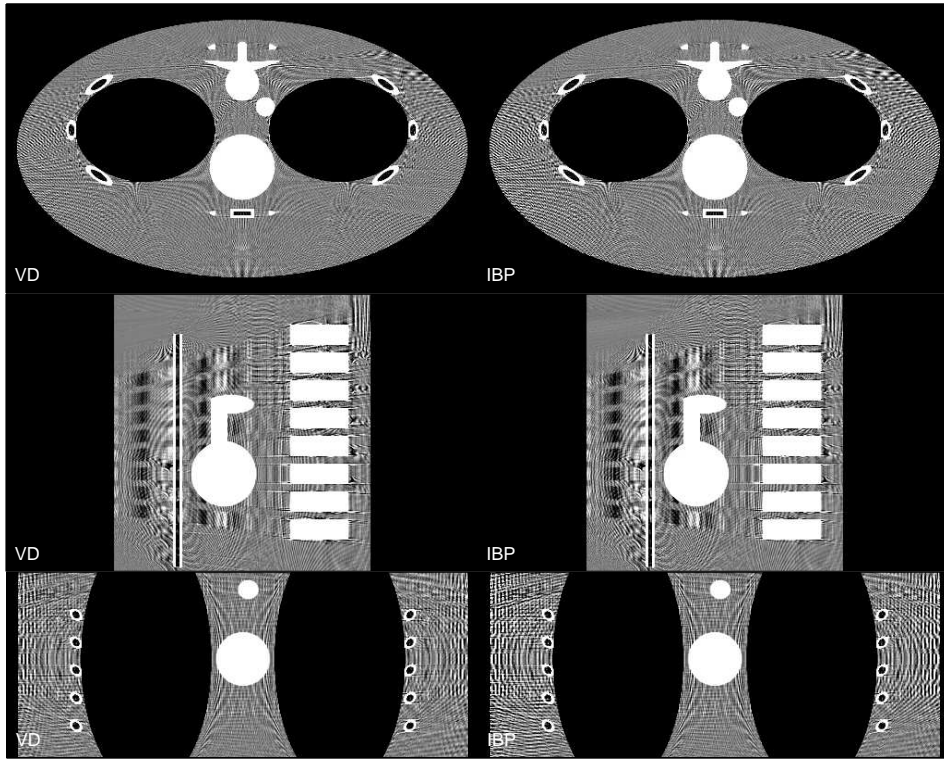


Fig. 5. Slices $z = 0$ mm (top), $x = 0$ mm (middle) and $y = 20$ mm (bottom) through the modified FORBILD thorax phantom without noise. Window: $[-20;20]$ HU.

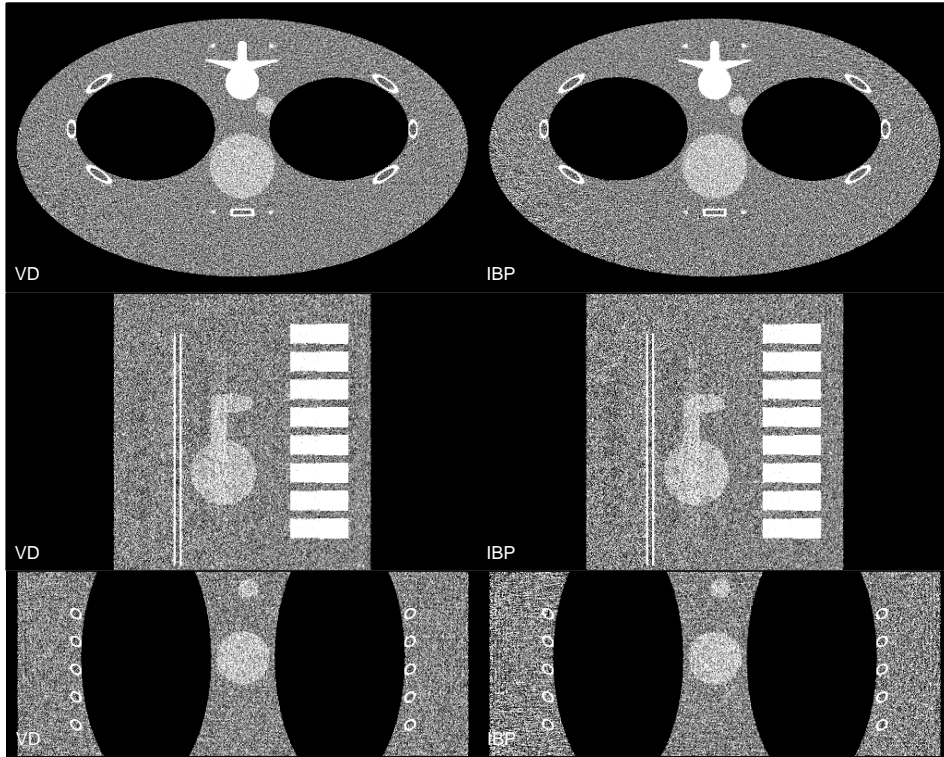
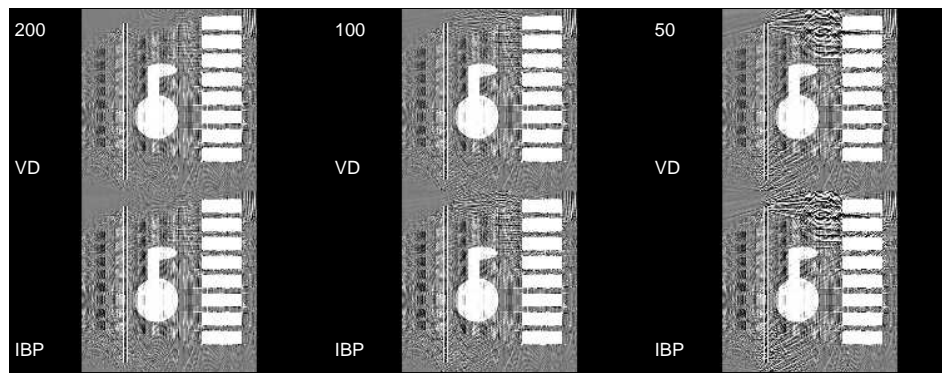


Fig. 6. Slices $z = 0$ mm (top), $x = 0$ mm (middle) and $y = 20$ mm (bottom) through the modified FORBILD thorax phantom from one realization of Poisson noise (150000 photons). Window: $[-100;100]$ HU.

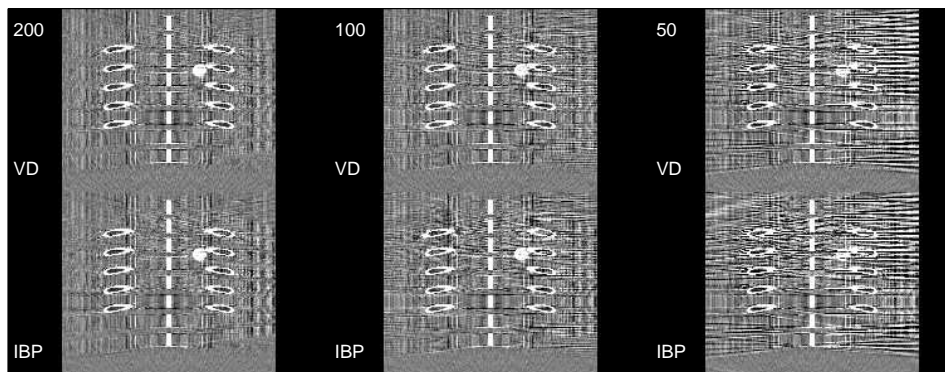
IV. CONCLUSIONS

We evaluated two cone-beam reconstruction formulae for the circle-plus-line trajectory in terms of resolution perfor-

mance, noise performance, visual image quality, computational effort and the impact of z -sampling on the line segment. The experiments show that the IBP approach offers a slightly

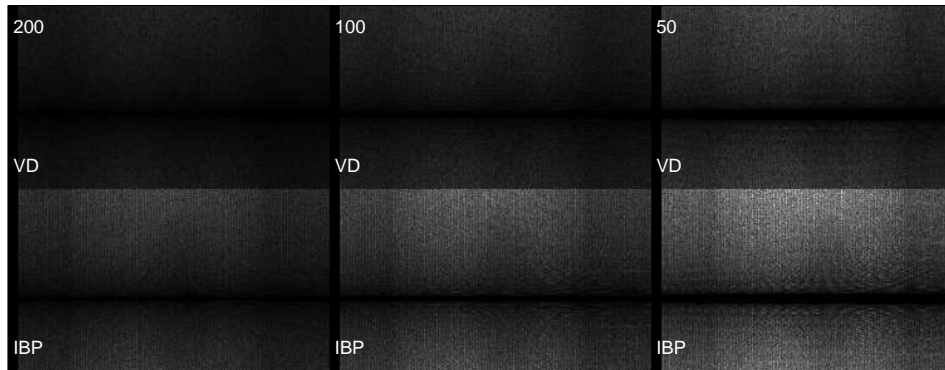


(a)

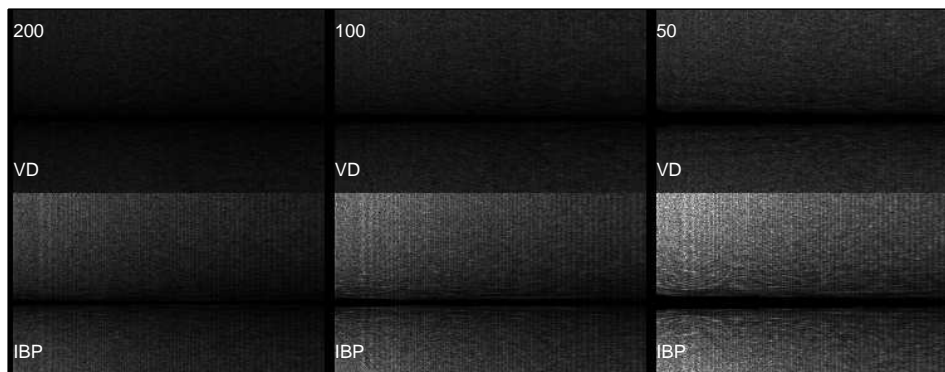


(b)

Fig. 7. (a) The slice $x = 0$ mm and (b) the slice $y = -80$ mm of the modified FORBILD thorax phantom is shown. Window: $[-40;40]$ HU.



(a)



(b)

Fig. 8. (a) The standard deviation images of the slice $x = 0$ mm and (b) the slice $y = -80$ mm of the modified FORBILD thorax phantom are shown.

higher resolution, especially in remote off-center regions. On the other hand, the VD formula using the new differentiation scheme offers a significantly lower standard deviation than the IBP formula in those regions. Discretization errors appear to impact image quality in the same way for VD and IBP. Noise propagation is however quite different. The VD formula offers a significant variance reduction in off-center regions. Moreover, the VD formula allows an improvement of almost a factor of two with respect to the computational effort. Also, the VD formula is easier to implement, compared to the much more complex IBP formula. The varying z-sampling on the line segment showed that the VD formula can be as robust as the IBP formula when the sampling rate is reduced.

Given those arguments, we may conclude that the VD formula using the new view differentiation scheme appears to be more attractive than the IBP formula despite the front-end requirement for view differentiation.

ACKNOWLEDGMENTS

This work was supported by Siemens AG, Medical Solutions and was supported in part by the U.S. National Institutes of Health (NIH) under grant R01 EB000627.

DISCLAIMER

The concepts and information presented in this paper are based on research and are not commercially available.

REFERENCES

- [1] A. Katsevich. Analysis of an exact inversion algorithm for spiral cone-beam ct. *Physics in Medicine and Biology*, 47(15):2583–2597, 2002.
- [2] H. Yang, M. Li, K. Koizumi, and H. Kudo. View-independent reconstruction algorithms for cone beam ct with general saddle trajectory. *Physics in Medicine and Biology*, 51(15):3865–3884, 2006.
- [3] A. Katsevich, K. Taguchi, and A.A. Zamyatin. Formulation of four katsevich algorithms in native geometry. *IEEE Transactions on Medical Imaging*, 25(7):855–868, 2006.
- [4] G.-H. Chen, R. Tokalkanahalli, T. Zhuang, B.E. Nett, and J. Hsieh. Development and evaluation of an exact fan-beam reconstruction algorithm using an equal weighting scheme via locally compensated filtered backprojection (lcfbp). *Medical Physics*, 33(2):475–481, 2006.
- [5] A. Katsevich, G. Lauritsch, H. Bruder, T. Flohr, and K. Stierstorfer. Evaluation and empirical analysis of an exact fbp algorithm for spiral cone-beam ct. *SPIE Medical Imaging 2003*, 5032:663–674, 2003.
- [6] F. Noo, S. Hoppe, F. Dennerlein, G. Lauritsch, and J. Hornegger. A new scheme for view-dependent data differentiation in fan-beam and cone-beam computed tomography. *Physics in Medicine and Biology*, 52(17):5393–5414, 2007.
- [7] A. Katsevich. Image reconstruction for the circle-and-line trajectory. *Physics in Medicine and Biology*, 49(22):5059–5072, 2004.